AIP Journal of Applied Physics

Temperature evolution of defects and atomic ordering in Si1−xGex islands on Si(001)

M.-I. Richard, A. Malachias, M. Stoffel, T. Merdzhanova, O. G. Schmidt, G. Renaud, T. H. Metzger, and T. U. Schülli

Citation: Journal of Applied Physics **119**, 085704 (2016); doi: 10.1063/1.4942530
View online: http://dx.doi.org/10.1063/1.4942530
View Table of Contents: http://scitation.aip.org/content/aip/journal/jap/119/8?ver=pdfcov
Published by the AIP Publishing

Temperature evolution of defects and atomic ordering in $Si_{1-x}Ge_x$ islands on Si(001)

M.-I. Richard,[1,2] A. Malachias,[3] M. Stoffel,[4] T. Merdzhanova,[5] O. G. Schmidt,[6] G. Renaud,[7] T. H. Metzger,[8] and T. U. Schülli[1]
[1]*ID01/ESRF, 6 rue Jules Horowitz, BP220, F-38043 Grenoble Cedex, France*
[2]*Aix-Marseille University, IM2NP-CNRS, Faculté des Sciences de St Jérôme, 13397 Marseille, France*
[3]*Departamento de Física, Universidade Federal de Minas Gerais, CEP 31270-901 Belo Horizonte, M.G., Brazil*
[4]*Institut Jean Lamour, UMR CNRS 7198, Université de Lorraine, BP 70239, F-54506 Vandoeuvre-Lès-Nancy, France*
[5]*Institut für Energie- und Klimaforschung (IEK-5), Forschungszentrum Jülich GmbH, 52425 Jülich, Germany*
[6]*Institute for Integrative Nanosciences, IFW Dresden, Helmholtzstrasse 20, D-01069 Dresden, Germany*
[7]*CEA, INAC-SP2M, F-38000 Grenoble, France*
[8]*Max Planck Institute of Colloids and Interfaces, D-14424 Potsdam, Germany*

(Received 8 October 2015; accepted 9 February 2016; published online 24 February 2016)

The observation of atomic ordering and signatures of defects in self-assembled Ge islands using x-ray diffraction techniques have been previously treated as unrelated subjects. However, mutual understanding can be achieved when both subjects are studied in a common frame. Here, we report on measurements and analysis of both defects and atomic ordering in $Si_{1-x}Ge_x$ islands epitaxially grown on Si(001) substrates as a function of growth temperature. By using x-ray diffraction and mapping around a bulk forbidden reflection, defect sizes, and in-plane spacing between nearby dislocations are extracted and related to the composition of the islands. The results fit well with an independent determination using selective wet chemical etching and atomic force microscopy measurements. Moreover, the temperature dependence of the ordered domain size is discussed. Although both atomic ordering and defect formation take place independently in the system, it is found that the relaxation provided by the onset of defects does not affect the formation of ordered domains, recently pointed out to be stabilized by strain and surface equilibrium on islands facets.
 [http://dx.doi.org/10.1063/1.4942530]

I. INTRODUCTION

Strain driven self-assembly can be considered nowadays as one of the easiest ways to form nanostructures. Among the different strained material combinations investigated so far, the Ge/Si(001) system is often considered as a model system due to its simplicity. After completion of a 3–4 monolayer (ML) thick wetting layer, three-dimensional (3D) islands form as a result of partial strain relaxation. As the Ge coverage increases, at constant temperature, the coherent (i.e., defect-free) island morphologies are known to evolve from rough, unfaceted prepyramids, to truncated pyramids, pyramids, transitional domes, domes, and eventually to barns.[1–5] During the past several years, the compositional state of these islands has been the subject of numerous investigations using many different techniques (see Ref. 6 as a review). The results provide evidence of significant intermixing with Si coming either from the substrate or from surface diffusion.[7,8] In addition, x-ray studies reveal that part of the Ge and Si atoms belonging to dome-shaped islands—in which pronounced alloying takes place—exhibit long-range order of atomic species with the appearance of superstructure reflections at forbidden reciprocal lattice positions.[9,10] Such an atomic arrangement follows an in-plane organization previously observed in thin films.[11] By comparing SiGe islands grown by different techniques, surface diffusion and intermixing at steep facets were identified as key parameters for achieving atomic ordering.[10] This was recently confirmed by the work of Vantarakis *et al.*,[12] who demonstrated that ordering in dome-shaped islands, which is a surface-related phenomenon, is mainly due to thermodynamics of the growing facets. The main source of ordering is the {15 3 23} facets, while the {105} and {113} facets contribute less. In all these measurements, however, only coherent island ensembles were considered with a negligible fraction of islands containing defects. Since strain is a key issue in semiconductor nanostructures, it is crucial to understand the evolution of atomic ordering once the islands are partially or fully strain-relaxed.

When the Ge deposition is further increased and the amount of material deposited passes a given threshold, the islands reach sizes at which it becomes energetically favourable to introduce dislocations. The onset of plastic relaxation can be recognized when large superdomes are observed to form[1,4,13,14] in addition to elastic strain relaxation still present in coherent islands. The critical size for dislocation introduction has been a long standing problem, which has been addressed both theoretically[15,16] and experimentally.[13,14,17] *In situ* transmission electron microscopy (TEM)[13,14] observations of superdome growth have revealed an intriguing cyclic growth mode. The islands grow vertically but suddenly expand laterally each time a new dislocation is introduced. Atomic force microscopy (AFM) measurements[17]

performed after selective wet chemical etching of the islands revealed nearly concentric ring-like structures similar to tree-rings, confirming thus the cyclic growth mode. In addition, recent investigations showed that the rings are regularly spaced (except for the first ring) forming a regular network of dislocations.[18] The spacing between rings was measured by AFM and corroborated by He ion microscopy characterizations. A simple model taking into account the energy gain, the energy cost, as well as the interactions between neighbouring dislocations was able to predict correctly the spacing between the rings. The ring spacing was, however, experimentally determined once the islands were etched by considering the footprints left by the islands on the surface.

Different types of dislocations can be found in SiGe superdomes, and their differences can be ascribed mainly to the growth temperature. At high temperatures ($T > 600\,^{\circ}C$), 60° type-dislocations are usually introduced. This temperature range was also found to induce atomic ordering of Si and Ge atoms inside the resulting islands. At low temperatures, however, the islands grow relaxed from the outset with pure edge dislocations[14] such as 90° Lomer type-dislocations. The latter can be dissociated into two partial dislocations and stacking-faults. Both of them accommodate misfit strain at the Ge/Si interface as dislocations at the interface reduce the total free energy of growing islands.[19] Finally, dislocated islands also contain {111} stacking-faults, which nucleate at the Ge/Si interface and can be found at any temperature when island formation is observed.[20]

Diffuse scattering of x-rays has been successfully used for the detailed investigation of defects in two-dimensional (2D) layers or crystals.[21,22] Exact analytical expressions have been given for the scattering of defects very close to Bragg reflections.[23,24] However, close to allowed Bragg reflections, the investigation of the structure of defects inside 3D islands is either difficult or impossible: the scattering contribution of defects inside 3D islands is weak due to the small number of atoms forming the defect and is thus hidden by the broad diffuse scattering from the nanostructures. Similarly to TEM,[25,26] we have demonstrated that the use of forbidden reflections in x-ray diffraction made possible the detection of defect types, their average size, and strain field inside Si crystals,[27] as well as in Ge islands grown on Si(001).[28] The technique makes it possible to study planar faults (stacking-faults), twin faults in nanostructures, and the structure of the core of defects in a Si crystal. Since some forbidden reflections are also able to detect atomic ordering of Si/Ge species, one can pick up a reciprocal space condition in which both signatures show up, allowing a direct evaluation of both phenomena.

In this paper, we consider island ensembles consisting of both coherent and dislocated islands with a significantly larger fraction of dislocated islands. We show that mapping around the bulk forbidden (200) reflection allows us to determine the temperature dependence of the size of both atomically ordered domains and defects as well as in-plane spacing between nearby dislocations while still preserving the islands. It also permits to relate these results to the composition of the islands. The obtained results fit well with an independent determination using selective wet chemical etching and extensive atomic force microscopy measurements. How ordering and defects can be correlated inside the nanostructures will be discussed. This shows that x-ray diffraction can provide useful structural information without the need of destructing the islands. The paper is organized as follows: after giving some experimental details on the growth and characterization techniques (Section II), we discuss the morphology of the islands (Section III A), the analysis of defects using the forbidden (200) reflection (Section III B), the dislocation network (Section III C), the island strain field (Section III D), and finally, the atomic ordering and surface kinetics (Section III E). The results are discussed in Section IV before summarizing (Section V).

II. EXPERIMENTAL

The samples studied in this work were grown by solid source molecular beam epitaxy on p-type Si(001) substrates having a very low miscut (less than 0.1°). After deoxidation at 950 °C, the substrate temperature was ramped down to 460 °C, and a 100 nm thick Si buffer layer was grown at a rate of 0.1 nm/s while ramping the substrate temperature from 460 °C to the desired island growth temperature. After a 5 s growth interruption, 15 ML of Ge were deposited with a growth rate of 0.03 ML/s at a fixed substrate temperature in the range from 620 °C to 800 °C. The samples were studied both by x-ray diffraction measurements and extensive atomic force microscopy measurements with selective wet chemical etching. One piece of each sample was etched with a mixture of ammonium hydroxide and hydrogen peroxide, $NH_4OH:H_2O_2$ (1:1), or in a buffered solution of hydrofluoric acid, hydrogen peroxide, and acetic acid, $HF:H_2O_2:CH_3COOH$ (1:2:3), namely, BPA.[29] These etchants are known to selectively remove $Si_{1-x}Ge_x$ over Si.[30,31] The surface morphology was then imaged by a commercial open-loop AFM operated in tapping mode. We used Si tips having a radius of curvature of approximately 5 nm. We chose scanning parameters to limit as much as possible scanning artifacts. Other pieces of the same samples were studied by grazing-incidence x-ray diffraction (GIXD) at beamline ID01 (ESRF). A monochromatic x-ray beam of 11 keV (wavelength λ of 1.1271 Å) was used. The suppression of the contributions of the higher harmonics of the x-ray beam was achieved by two mirrors. All samples were illuminated at a grazing angle of 0.14°, below the critical angle of total external refection for Si ($\alpha_c = 0.161°$). This condition establishes a penetration depth of few tens of nanometers, allowing for a partial suppression of the signal from the Si substrate, and a relative enhancement of the signal diffracted by the Ge islands. The exit angle α_f was collected from 0° to 1.5° by a linear Position Sensitive Detector (PSD) perpendicular to the sample surface. All direct- or reciprocal-space notations refer to the bulk Si unit cell $a_{Si} = b_{Si} = c_{Si} = 5.431$ Å and $\alpha = \beta = \gamma = 90°$. The Miller indexes ($h$, k, and l) are expressed in reciprocal-lattice units (r.l.u.) of Si. The average island composition (x_{Ge}) determined using x-ray anomalous diffraction is $\sim(50\pm5)\%$, $\sim(40\pm5)\%$, $\sim(35\pm5)\%$, and $\sim(32\pm5)\%$ at 620 °C, 700 °C, 740 °C, and 800 °C, respectively, in good agreement with the results obtained by AFM.[18]

III. RESULTS

A. Atomic force microscopy

Figures 1(a)–1(c) show AFM images obtained upon deposition of 15 ML of Ge on Si(001) at three growth temperatures. One can recognize different island morphologies such as coherently strained domes (D) and barns and larger, multifaceted superdomes (SD). The main differences between the samples are the island average size and density, which increases and decreases with temperature, as a result of larger SiGe intermixing and coarsening. Both coherent barns and superdomes exhibit {111} facets at their periphery.[32] Figure 1(d) displays the evolution of the average {111} island facet size and the average diameter of coherent islands measured by AFM. They were calculated by averaging the values measured by AFM over an area of $8 \times 8\,\mu m^2$. First, AFM images in which the contrast is proportional to the local surface slope with respect to the (001) plane allow the identification of the 111 facets close to the island base. Taking z-profiles of individual islands further identifies them. Figures 1(e) and 1(f) display the z-profile of one of the superdomes grown at 620 °C and 700 °C, respectively. These slope histograms highlight the {111} facets at the periphery of the superdomes. We then compute, for each island contained in the AFM image, the area of the 111 facets. The obtained values were then corrected assuming a convolution between the real sample surface and the tip shape (radius of curvature of about 5 nm). Both the average {111} island facet size and the average diameter of coherent islands increase with temperature. The facet size tends to scale with the island base diameter. The evolution of the {111} facets is discussed here to compare it in the following with the evolution of the size of the {111}-type defects.

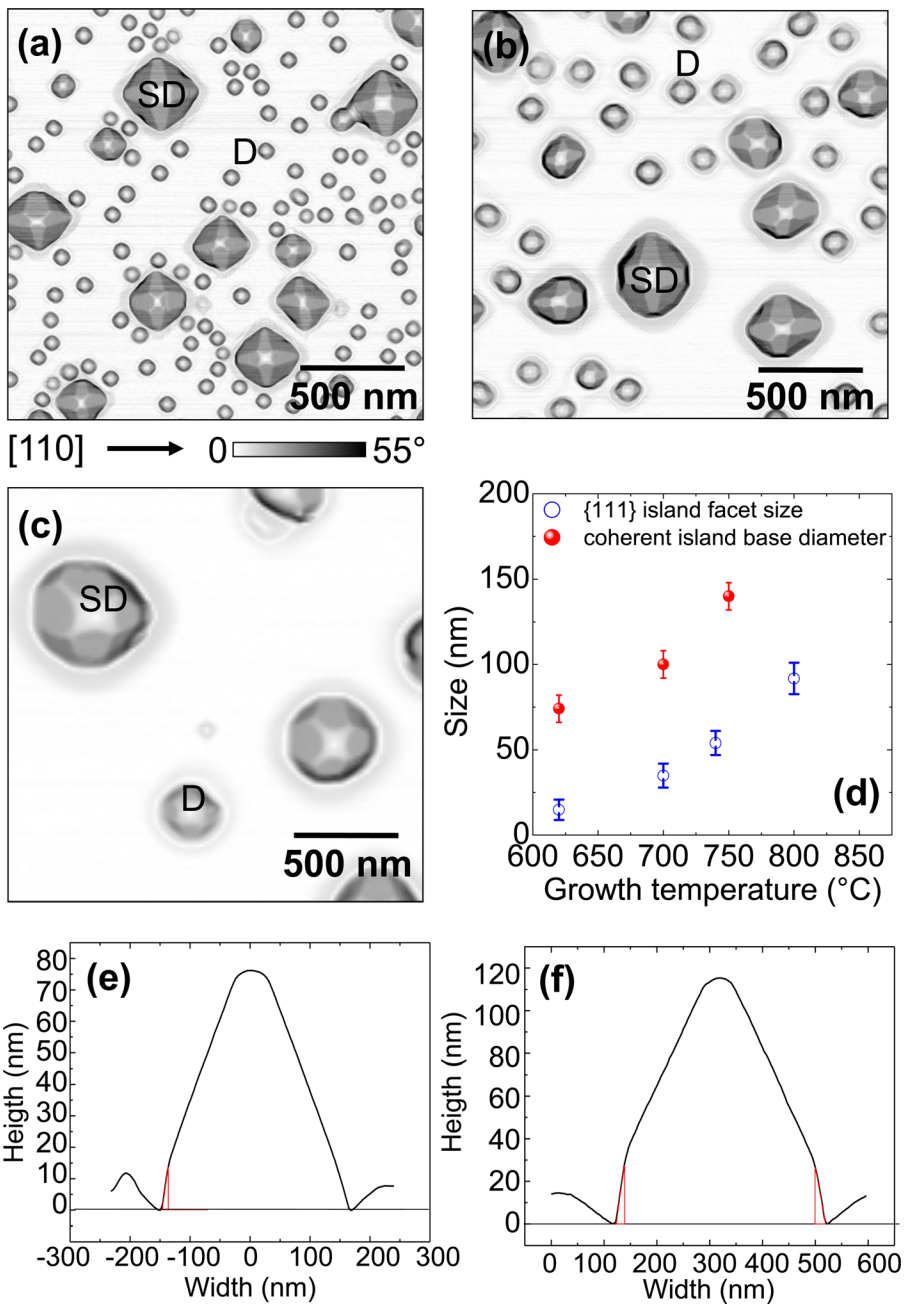

FIG. 1. AFM images taken after deposition of 15 ML Ge at 620 °C (a), 700 °C (b), and 800 °C (c). Most of the islands are coherent domes (D) and superdomes (SD). The color scale, which indicates the slope, applies to the three AFM images (a)–(c). (d) Evolution of the average {111} island facet size and coherent island average base diameter for different growth temperatures. The shading allows steep and shallow facets to be distinguished according to the local surface slope with respect to the (001) plane. (e) and (f) z-profile of one of the superdomes grown at 620 °C and 700 °C, respectively.

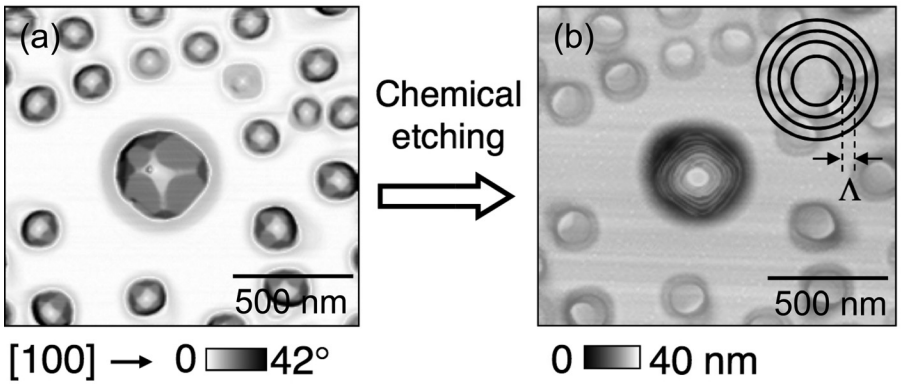

FIG. 2. Example of AFM images of the same surface area prior to (a) and after (b) selective wet chemical etching in a BPA solution (deposit of 15 ML Ge grown at 800 °C). The color scales in the left and right panels correspond to slope and height, respectively. The average distance between the tree-ring structures is noted Λ.

Figure 2 shows AFM images of the same surface area measured before and after selective wet chemical etching in a BPA solution. The dislocated islands leave behind a complex footprint with a tree-ring structure on the surface. The tree-ring structure consists of neighboring circular plateaus all surrounded by nearly concentric rings (see inset of Fig. 2(b)). The central Si plateau is interpreted as the original island base prior to introduction of the first dislocation. The different concentric rings are explained as a result of the cyclic growth mode,[17] in which an island rapidly expands in lateral direction after introduction of a dislocation and then grows without lateral expansion until the next dislocation is introduced. The distance Λ between the different concentric rings (see inset of Fig. 2(b)) gives an estimation of the average distance between dislocations inside the islands.

B. Analysis of defects using the (200) forbidden reflection

Measurements in the vicinity of basis-forbidden reflections can reveal details about the presence of defects in Si/Ge crystals.[27,28] In particular, the structure factor of a non-deformed unit cell at the (200) reflection verifies $F_0(200) = 0$ in Si and Ge. This is therefore a suitable position in reciprocal space to look either for defect scattering or atomic ordering.

Figures 3(a) and 3(b) display the three dimensional intensity distribution around the diamond unit cell basis-forbidden (200) reciprocal space position, where the l direction represents the intensity distribution along the linear detector, for islands grown at two different temperatures. In these reciprocal space maps, the scattered intensity is concentrated in streaks along the ⟨111⟩ directions. According to previous studies,[27,28] the rod-like intensity along ⟨111⟩ is a characteristic of {111} stacking-faults (SFs) or twin faults. Figure 3(c) shows a scheme of a {111} stacking-fault, which lies in {111} planes, displaying the $\langle 1\bar{1}0\rangle$ and $\langle 11\bar{2}\rangle$ crystallographic directions useful for its characterisation using x-ray scattering.

To quantify the evolution of the average size of the {111}-type defects as a function of growth temperature, the full width at half maximum of the streaks was fitted along the $\langle 1\bar{1}0\rangle$, $\langle 11\bar{2}\rangle$, and ⟨111⟩ directions using a sum of

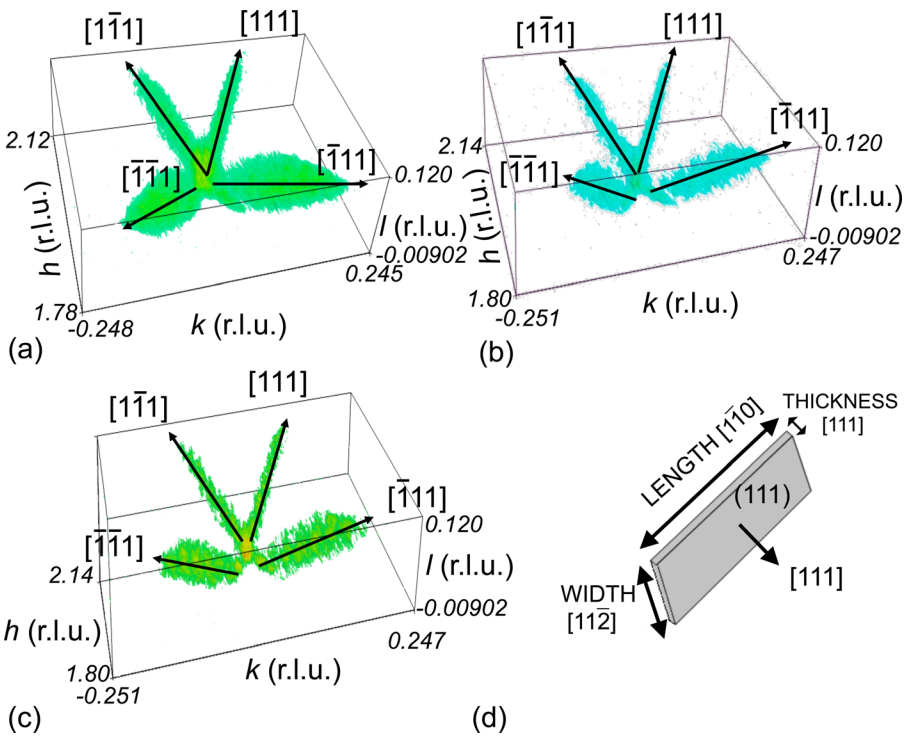

FIG. 3. Three dimensional intensity distribution around the (200) forbidden reflection (logarithmic scale). The scattered intensity is concentrated in streaks along ⟨111⟩ directions for samples grown at 620 °C (a), at 700 °C (b), and at 740 °C (c), respectively. (d) A scheme of a {111} stacking-fault showing the crystallographic directions useful for its characterisation using x-ray scattering.

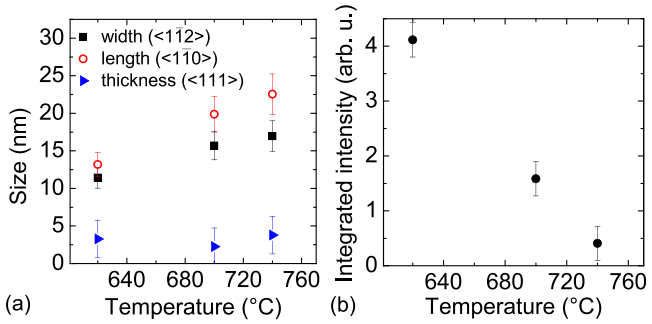

FIG. 4. Evolution of the size (a) and of the integrated intensity (b) of the {111} stacking-faults as a function of growth temperature.

three-dimensional Gaussian functions. This makes it possible to estimate the average size of the {111}-type defects as a function of temperature. The results are shown in Fig. 4(a). Note that the signal was too weak to fit the rod-like intensities observed for the sample grown at 800 °C. In Figs. 3(a) and 3(b), the reciprocal space width of the streaks decreases with increasing temperature, meaning that the size of the {111}-type defects in the {111} planes increases with temperature as observed in Fig. 4(a). For instance, the length of the {111}-type defects increases from 13 ± 5 nm at 620 °C to 21 ± 5 nm at 740 °C. The {111} rod-like scattering in the vicinity of the (200) reflection could also be the signature of scattering by the {111} facets located close to the base of the barns/superdomes. However, the average size of the {111} facets plotted in Fig. 1(d) is up to three times larger than the size obtained by the fit of the streaks, indicating thus that the rod-like intensity at this reciprocal space condition is not coming from the {111} island facets.

The analysis of the streaks in the ⟨111⟩ directions also offers the possibility to get a qualitative insight of the relative number of defects tied up in stacking-faults from the integrated intensity of the streaks. Figure 4(b) displays an estimation of the average integrated intensity of the {111}-type defects as a function of growth temperature. A decrease in the integrated intensity is observed with temperature, implying that the number of {111}-type defects are decreasing with temperature. At higher temperatures, the decrease of the number of {111}-type defects could be due to material transport (coarsening), as the density of islands decreases with temperature (see Figs. 1(a)–1(c)) and/or possibly by self-healing of the stacking-faults. Figure 5 displays the reciprocal space maps around the basis-forbidden (200) and allowed (400) Bragg peaks for all investigated samples. The intensity was integrated along *l*, i.e., along the [001] direction. Consequently, close to the basis-forbidden (200) reflection, the integrated hump-like intensity follows the projected ⟨110⟩ directions in the plane. The integrated intensity coming from the {111}-type defects is clearly decreasing as a function of growth temperature.

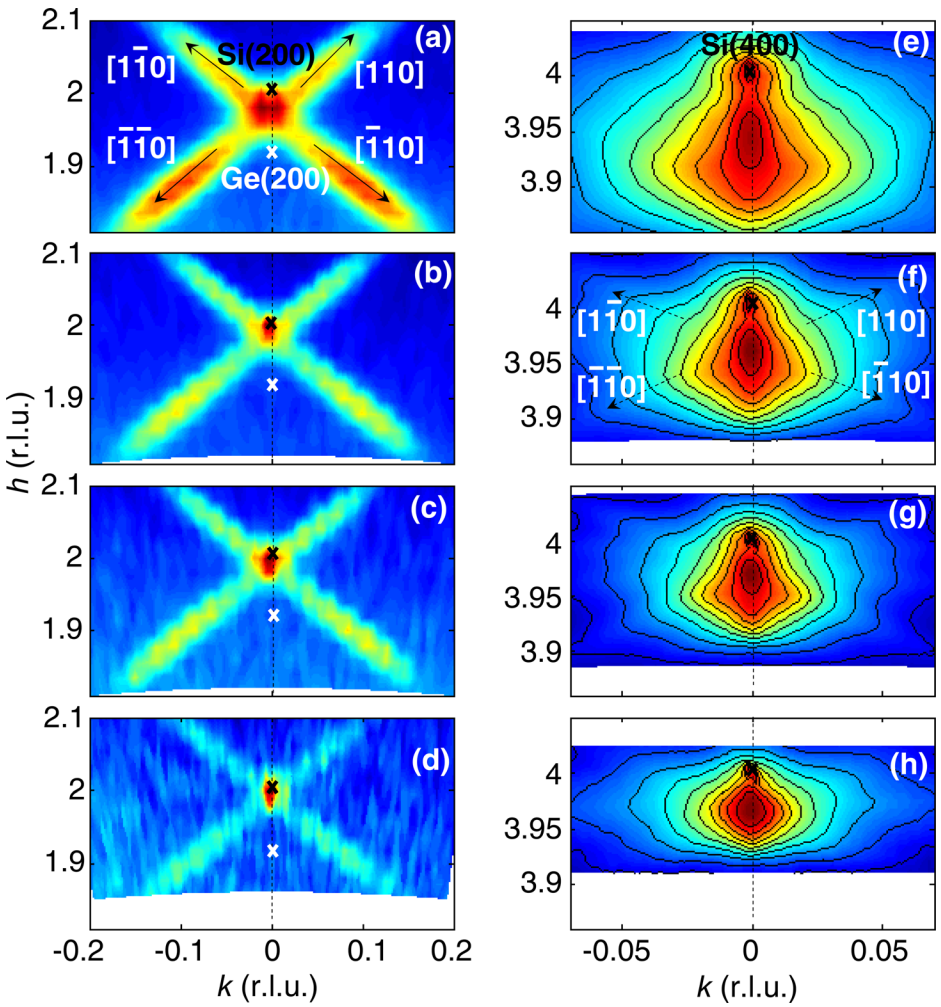

FIG. 5. (a)–(d) (200) reciprocal space maps for the four samples grown at a temperature of 620 °C, 700 °C, 740 °C, and 800 °C, respectively. The signal is concentrated in streaks along ⟨111⟩, i.e., along ⟨110⟩ in the plane after integrating the signal along the [001] direction. (e)–(h) (400) reciprocal space maps with contour levels for the four samples grown at a temperature of 620 °C, 700 °C, 740 °C, and 800 °C, respectively. One part of the signal is also concentrated in streaks along ⟨111⟩, i.e., along ⟨110⟩ in the plane after signal integration along [001]. The black and white crosses indicate the position of the (200)Si or (400)Si Bragg and the (200)Ge peak at $h \sim 1.917$, respectively. The position of (400)Ge peak is out of the frame in Figs. 5(e)–5(h). The dashed lines denote the trajectory, along which the line scans in Fig. 6 were performed.

Close to an allowed Bragg reflection **G**, the defects can cause an asymmetry of the diffuse scattering (usually called Huang scattering) along the $q_r(= 4\pi/\lambda \sin(2\theta/2)$, where 2θ is the scattering angle) direction, which is strain sensitive. This provides information about the sign of the long-range distortion field of the lattice structure surrounding the defects.[33] The scattering from interstitial-type defects, which expand the lattice, exhibits a higher diffuse intensity I for $\mathbf{G}.\delta\mathbf{q_r} > 0$ ($\delta\mathbf{q_r}$ being the deviation of a point in the reciprocal space along the $\mathbf{q_r}$ direction from the Bragg reflection **G**), while the opposite happens for vacancy-type defects, which contract the lattice.

On the contrary, close to forbidden reflections, the displacement-scattering term can be neglected and the diffuse scattering stems only from the defect cores, i.e., by the atomic positions in the defect cores.[27] Interstitial-type defects result from a local lattice compression and will exhibit a higher diffuse intensity for $\mathbf{G}.\delta\mathbf{q_r} < 0$ in contrast with allowed Bragg reflections. The opposite will be observed for vacancy-type defects. The asymmetric intensity distribution of the streaks with higher intensity for $\mathbf{G}.\delta\mathbf{q_r} < 0$ (see Figs. 5(a)–5(d)) indicates that the {111} defects are interstitial-type defects and proves the extrinsic nature of the stacking-faults.

In a cubic diamond structure, extrinsic stacking-faults (ESFs) are formed when two additional {111} atomic layers are inserted into the lattice. As a consequence, the ESFs lie in {111} planes and consist of two parallel {111} planes separated by the distance Δ. From previous results, it follows that the two inserted planes which form the extrinsic stacking-faults are compressed: $\Delta - \Delta_0 < 0$, where Δ and Δ_0 are the experimental and nominal distances between the two inserted planes forming the stacking-fault. Note that, for instance, $\Delta_0 = a_{Si}\sqrt{3}/4$ if the stacking-faults are bounded by Frank loops with Burgers vector $\mathbf{b} = a_{SiGe}/3\langle 111\rangle$, where a_{SiGe} is the average island lattice parameter (see Ref. 28 for details).

Intensity streaks are less visible in the reciprocal space maps around the allowed (400) Bragg reflection. Nevertheless, in Figure 5(f), where the diffracted intensity has been integrated along the l-direction, it can be observed that a part of the diffuse scattering is concentrated in intensity streaks along the $\langle 110\rangle$ directions. A three-dimensional intensity map (not shown here) reveals that the intensity streaks along $\langle 110\rangle$ are projections of $\langle 111\rangle$ streaks on the $\langle 110\rangle$ directions in the {001} plane. The signal could come from diffuse scattering either from {111} stacking-faults or {111} facets. From the fit of the width of the $\langle 111\rangle$ rods, which gives a size of ~39 nm for the sample grown at 700 °C, it follows that the diffuse scattering near the (400) reflection comes from the {111} facets of the islands, since the determined value is in good agreement with the facet size measured by AFM (see Fig. 1(d)). The (400) allowed reflection is sensitive to the form factor of the islands, whereas the (200) forbidden reflection is sensitive to the local truncation of the unit cell symmetry (induced, for instance, by defects).

C. Dislocation network

The evaluation of reciprocal space positions and widths for the (200) scattering features allows for obtaining structural parameters related to the defects inside islands which contain dislocations. The superdomes are characterized by misfit dislocations (MDs) at the island/substrate interface. If we assume that the effective strain induced by defects is given by the average relaxation of defects observed at the (200) forbidden reflection, then the average in-plane distance between two dislocations is $\Lambda = b_{\text{eff}}/\epsilon_{200}$,[34] where b_{eff} is the effective Burgers vector of the dislocations, and ϵ_{200} is the average strain value measured from defects at the (200) forbidden reflection. 60° dislocations are commonly observed in SiGe islands at high growth temperatures.[13,14] Their effective Burgers vector contributing to the in-plane relaxation is $b_{\text{eff}} = \frac{a_{SiGe}}{\sqrt{2}}\cos(\pi/3)$.[18]

To access the average strain of defects with respect to the Si substrate, ϵ_{200}, which is given by $\Delta h/h_{Si}$, i.e., here $(h_{200} - 2)/2$, the h_{200}-position of the center of the "X" features (see Figs. 5(a)–5(d)) was determined. The h_{200}-position also corresponds to the h value at the maximum of intensity of the peaks observed at the (200) forbidden reflections in Fig. 6(a), where the radial scans around the (200) forbidden reflection are displayed. The trajectory of the radial scans is shown as a dashed line in Figs. 5(a)–5(d). The absolute value of ϵ_{200} changes with temperature and decreases from 1.84% at 620 °C to 0.71% at 800 °C. The in-plane distance between two interfacial 60° dislocations then evolves from 11 ± 5 to 27 ± 5 nm with increasing temperature from 620 °C to 800 °C (see Fig. 7(b)).

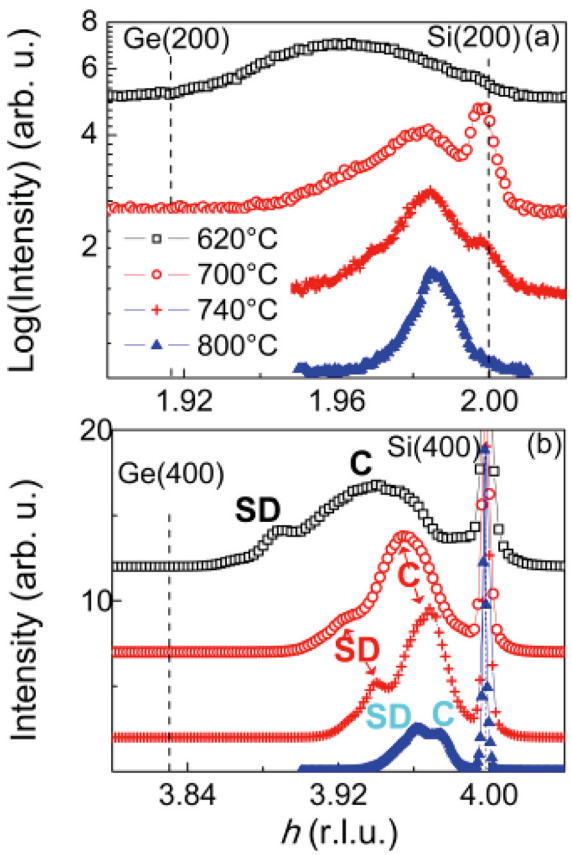

FIG. 6. Radial scans (shifted vertically to improve clarity) around the diamond unit-cell basis-forbidden (200) (a) and allowed (400) (b) reflections as a function of growth temperature. "C" and "SD" label the scattering positions of the coherent islands and superdomes.

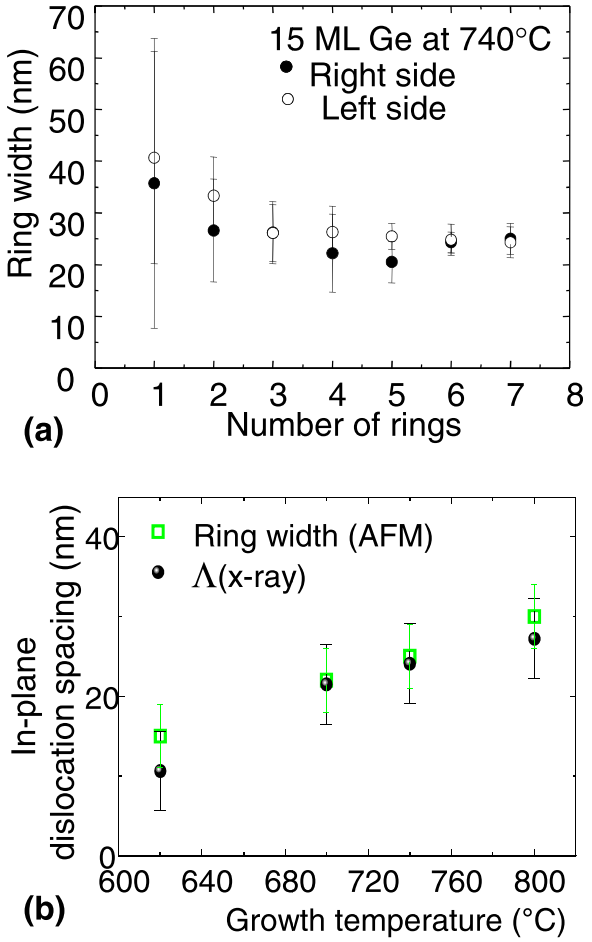

FIG. 7. (a) Statistical analysis of the ring width as a function of number of rings measured at the right and the left side of the central plateau from AFM microscopy images of a dozen of islands growth 740 °C. (b) Evolution of the inter-dislocation distance Λ given by etching (ring width) and x-ray diffraction.

Figure 7(a) displays the average ring width at the left and right sides of the central plateau (see Fig. 2) obtained from extensive measurements on a sample grown at 740 °C. The first value of the ring width corresponds to the island base diameter before the introduction of the first dislocation so that variation in size is expected depending on the different conditions occurring at the very first plastic event. The ring width after the injection of the first dislocation has been revealed as a good estimation of the average distance between dislocations.[18] The evolution obtained from x-ray diffraction fits well with this independent determination based on combined selective wet chemical etching and extensive AFM measurements of the ring width versus number of rings of the SiGe islands (see Fig. 7(b)). The distance between dislocations increases with temperature, meaning that intermixing delays the formation of dislocations. Recently, a model, which includes suitable energy gain and cost as well as mutual interactions between dislocations, was able to predict the spacing between tree-rings, i.e., the self-ordering of dislocations inside SiGe islands in a quasi regularly spaced network.[18]

D. Island strain field

The reciprocal space maps around the (400) Bragg reflection allow to infer the relaxation of the grown islands (see Figs. 5(e)–5(h)). The intensity along the radial direction clearly extends to lower h values (i.e., larger lattice parameters) for lower temperatures as a consequence of reduced SiGe intermixing. Such effect is shown in Fig. 6(b), where the radial scans around the (400) allowed reflection are displayed. In Fig. 6(b), at all temperatures, the diffuse signal is composed of two humps. The humps close to the Si(400) Bragg peak can be attributed to scattering from coherent defect-free islands (i.e., pyramids, domes, and barns). The hump signal closer to the position of the Ge Bragg peak ($h \sim 3.834$) originates from partially strain-relaxed islands, such as dislocated superdomes. Indeed, the larger lattice parameter of these islands, closer to the value for bulk Ge if compared to the coherent island hump position, can only be explained by the occurrence of plastic relaxation as coherent islands are much more strained by the Si substrate. The same effect was also reported on InAs:GaAs islands.[35]

The scattering from coherent islands and superdomes is labelled "C" and "SD" in Fig. 6(b). At the right side of the Si Bragg peak, the diffuse scattering is decreasing as a function of growth temperature. This signal can be associated with the diffuse scattering from Si atoms of the substrate in regions surrounding the islands that are subjected to compressive strain as higher values in reciprocal space imply smaller lattice parameters, i.e., compression. Consequently, the Si substrate is more compressed by the islands grown at lower temperatures having a higher Ge content. Figure 8(a) displays the evolution of the volume of the coherent and incoherent islands as well as the volume ratio of the incoherent/coherent islands as a function of temperature by fitting gaussian curves to the radial scan humps of the coherent islands "C" and superdomes "SD" in Fig. 6(b). The volume of coherent islands decreases with temperature, while the volume of superdomes increases. This can be explained by anomalous coarsening, with material being transferred from coherent islands to larger superdomes.[4]

The ability from x-rays to quantitatively depict the strain relief after the introduction of defects is discussed below. From the h position of the diffuse signal of the coherent islands and superdomes, their average in-plane elastic strain with respect to Si can be determined. The average in-plane elastic strain, $\epsilon_{//}$, of the dislocated islands is given by $\epsilon_{//} = \Delta a/a - b_{\text{eff}}/\Lambda$, where $\Delta a/a = \Delta h/h$ is the average lattice mismatch between the superdomes and the substrate. b_{eff}/Λ, i.e., the strain induced by the introduction of dislocations, can be calculated from the Λ values obtained at the (200) forbidden reflection or by selective wet chemical etching. The elastic strain of the coherent islands with respect to Si is directly given by $\Delta a/a = \Delta h/h$, which is calculated from the h position of the coherent island hump. These values are plotted as a function of temperature in Fig. 8. They all decrease as a function of temperature as a result of enhanced intermixing. The elastic relaxation of coherent islands and superdomes is rather comparable, meaning that when superdomes form, elastic relaxation stops being effective, and then plastic relaxation sets in. Our samples contain a significant fraction of dislocated islands coexisting with coherent islands. This enables us to distinguish separate contributions in the radial scans and thus to estimate separately the elastic strain relaxation for both coherent and dislocated

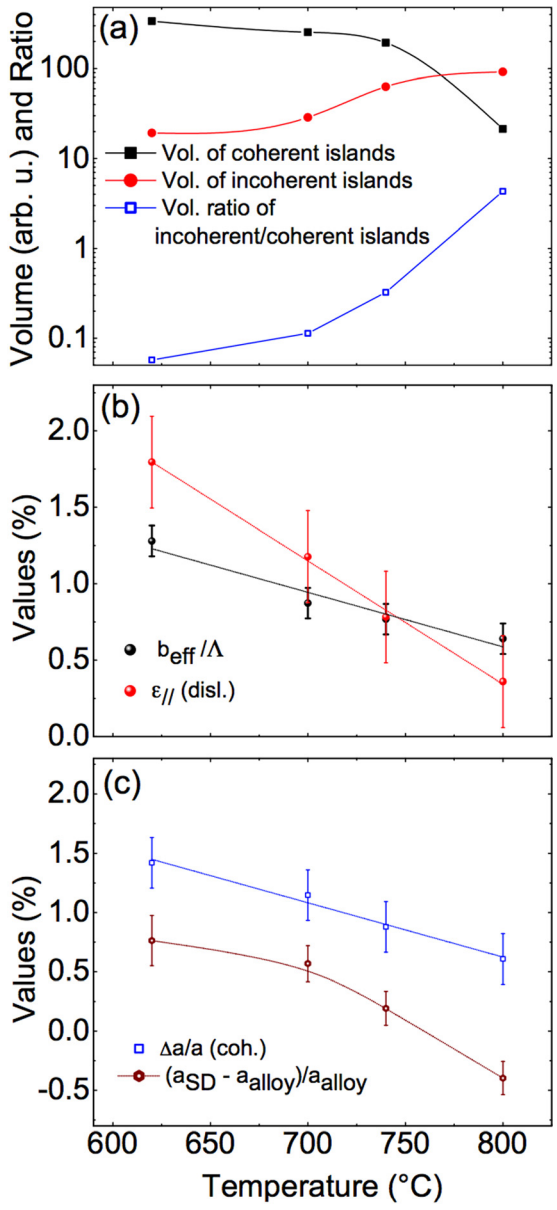

FIG. 8. (a) Volume of coherent and incoherent islands and volume ratio of incoherent/coherent islands obtained by fitting gaussian curves to the radial scan humps in Fig. 6(b). (b) Evolution of the average in-plane elastic strain $\epsilon_{//}$ (red) of the dislocated islands (disl.) and of b_{eff}/Λ (black) as a function of growth temperature. (c) Evolution of $\Delta a/a$ of the coherent islands (coh.) and of the average strain of superdomes, $(a_{SD} - a_{alloy})/a_{alloy}$, as a function of growth temperatures.

islands. This is a major result, which has not yet been obtained since in most cases only coherent island ensembles were analyzed. Figure 8(c) also displays the evolution of the average strain of superdomes given by $\epsilon_{SD} = (a_{SD} - a_{alloy})/a_{alloy}$, where a_{SD} and a_{alloy} are the average lattice parameter of the superdomes (provided by determining the center of mass of the peak of the superdomes in the radial scan) and the lattice parameter of a SiGe alloy having the same average Ge concentration as the superdomes, respectively. The average Ge concentration of the superdomes was obtained from anomalous diffraction at the (400) reflection. ϵ_{SD} provides quantitative information about strain in incoherent islands, demonstrating that they are not totally relaxed.

E. Atomic ordering and surface kinetics

For all samples, one observes a double-peak feature along the k transversal direction at the intersection of the $\langle 111 \rangle$ streaks in the (200) reciprocal space map. Figure 9(a), which corresponds to a zoom of the (200) reciprocal space map at the intersection of the $\langle 111 \rangle$ streaks for the sample grown at 700 °C, clearly displays the two-peak structure, which was previously observed by Malachias *et al.*[9] in

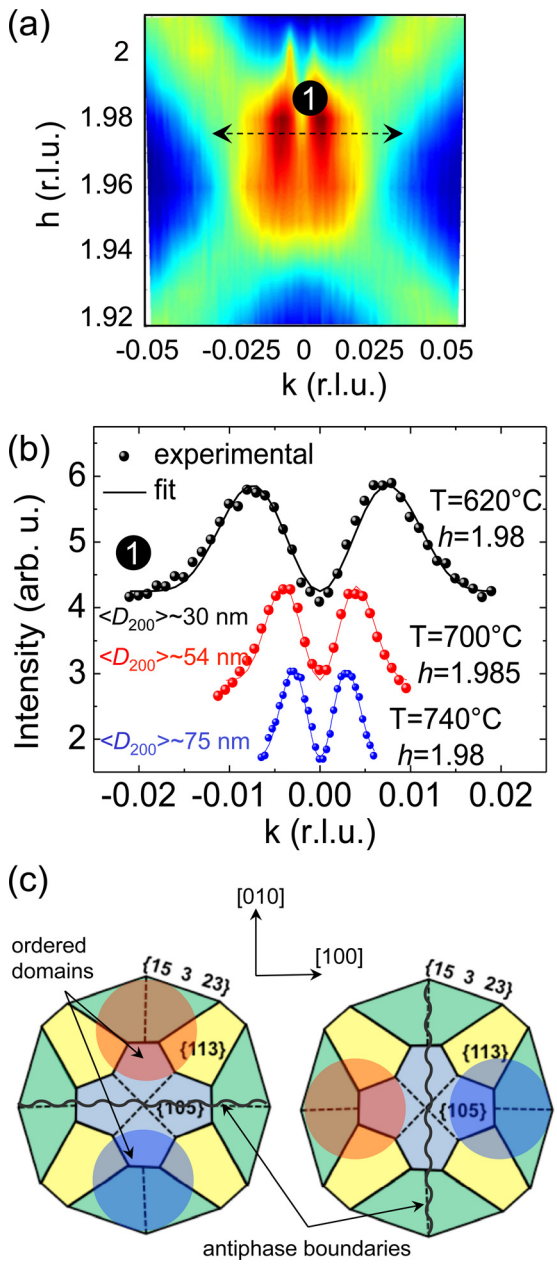

FIG. 9. (a) Zoom of the (200) reciprocal space map (sample grown at 620 °C) at the intersection of the $\langle 111 \rangle$ streaks, where signatures of ordered domains are observed. The dashed line labeled (1) denotes the trajectory, along which the line scan labeled (1) in Fig. 3(b) was performed. (b) Angular scans at the h position of maximum of intensity of the scattering from ordered domains for three growth temperatures. $\langle D_{200} \rangle$ indicates the average size of the ordered domains supposing two ordered domains along the [010] or [100] direction, which are separated by an antiphase boundary. (c) Models of dome-shaped islands with the three types of facets {105}, {113}, and {15 3 23} and of ordered domains (red and blue circles), which are separated by an antiphase boundary.

dome-like islands. The structure was described as the signature of chemically ordered alloys in SiGe islands, which are separated by antiphase boundaries. The antiphase boundaries explain the nodal plane observed at $k=0$. To evaluate the average size of the ordered alloy domains inside the SiGe islands, we suppose that the islands are only composed of at least two ordered domains, which are separated by an antiphase boundary along the [010] or [100] direction. As the same diffraction pattern is observed for all {200} types of reflection,[36] this implies that the model of domain distribution must follow a four-fold symmetry in real space, such as the one from steeper (high index) facets, with antiphase boundaries along the ⟨010⟩ directions to create the observed minimum at $q_a=0$. By contrast, no minimum of intensity is observed along the radial q_r direction, which is strain sensitive. The gradient of deformation and the distribution of domains and island sizes entail a broad scattering along the radial direction and may hide any minimum of intensity in this direction. Another possibility to obtain two distinct lobes without a minimum along the radial direction is that the sample is composed of two types of islands with ordered domains separated by either [100] or [010] anti-phase boundaries. As the initial surface is both 2×1 and 1×2 reconstructed and as atomic ordering may be linked to this initial surface reconstruction, these two types of islands may coexist. Summing incoherently the diffraction patterns of these two types of islands suppresses any minimum of intensity along the radial direction.

X-ray profiles along the [010] direction in reciprocal space measured at the maximum of intensity of the double-peak feature and at three temperatures are displayed in Fig. 9(b). The size D of the ordered domains was fitted using the following relation:[36]

$$A(q_a) \propto \frac{e^{iq_aD}-1}{e^{iq_aa_{Si}}-1} + e^{i(q_a(p+D)+\pi)}\frac{e^{iq_a(D+\Delta D)}-1}{e^{iq_aa_{Si}}-1}, \quad (1)$$

where $q_a = 2\pi.k/a_{Si}$ is the angular reciprocal space vector, and p is the size of the antiphase boundary, which separates the ordered domains. As we do not have pure order data, it is difficult to extract a value for p. We fix it to zero so that the value obtained for D corresponds to the maximum possible size of the ordered domains. The fits give an average maximum size of 30, 54, 75, and 160 nm for the samples grown at 620 °C, 700 °C, 740 °C, and 800 °C, respectively. The domains have just the size to fit two domains laterally arranged inside a coherent dome (see the measured average base diameter plotted in Fig. 1(d) and the drawing in Fig. 9(c), which shows one possibility of arrangement of the ordered domains inside the coherent domes). As already observed by Malachias *et al.*,[9] the size of the ordered domains increases with temperature probably as a result of the enlargement of the islands with intermixing. The integrated intensity of the curves gives an indication of the volume of the ordered domains. It is maximum at 620 °C, where the Ge composition of the islands has been found equal to 0.5, implying that a maximum degree of ordering is observed at 620 °C. Since previous works[12,36] point out the development of ordered domains in steeper facets, if four domains are in the same islands and separated by ⟨100⟩ antiphase boundaries, the measured size of the ordered domains would be too large to fit the domains in coherent islands, meaning that ordering would exist in dislocated islands. This means that from the average domain size measured ordering would also exist in dislocated islands, where steeper facet sizes still increase upon Ge deposition. In addition, for the samples studied in this work, the ordered domain size has shown no direct relation to the width of the defect-free region observed by AFM in the center of the islands (see Fig. 7(b)). In the samples grown at 700 °C, 740 °C, and 800 °C, the ordered domain size is larger than the width of the central defect-free region of the islands, and much larger than the ring widths found by AFM, indicating that the atomic ordering is not constrained nor suppressed by the introduction of defects. Hence, such observation supports the actual scenario discussed in Ref. 10, in which ordering arises as a result of surface kinetics driven alloying at the ⟨113⟩ and ⟨15 3 23⟩ steep island facets.[10] Interestingly, for all samples, the double-peak feature is localized at the same h position, which is at the intersection of the ⟨111⟩ streaks in the (200) reciprocal space maps. This reveals that the ordered domains are localized inside the same relaxed regions as the {111} stacking-faults, i.e., at the bottom part of the islands.

IV. DISCUSSION

From the data presented above, one can infer that two main informations can be extracted from the (200) forbidden reflections. First, the double-peak feature which has been associated to presence of ordered domains separated by antiphase boundaries. Second, the X-like features (not observed in defect-free islands by Malachias *et al.* in Ref. 9) are the signature of the presence of defects along the ⟨111⟩ directions.

For all growth temperatures, strain relaxation occurs elastically and plastically in superdomes, most notably by the generation of misfit dislocations for the second case, showing an important temperature dependency. The islands grown at low temperature show a higher gradient of relaxation than those grown at high temperature. Selective wet chemical etching studies have shown that the substrate surface topography under islands containing several dislocations is a quasi periodic structure which looks like annular rings of a tree. The ring period characterizes the average distance by which the lateral boundary of the island grows between two sequential dislocation events in the island, which allows to determine the in-plane distance between interfacial dislocations. This distance can also be determined by x-ray diffraction close to the (200) forbidden reflection, as demonstrated above. In addition to dislocations, the ⟨111⟩-type defects have been observed. Their size increases along the $\langle 1\bar{1}0\rangle$ and the $\langle 11\bar{2}\rangle$ directions as a function of growth temperature (see Section III A), obviously as a result of island enlargement with temperature. The number of ⟨111⟩-type defects were observed to decrease with temperature. All values quantified here and discussed above were retrieved by a non-destructive method. These last two results cannot be retrieved by any other experimental technique.

The origin of the stacking-faults is also a matter of discussion in the actual scenario. The stacking-faults can be associated with MDs at the interface as a part of dissociated MDs. Split threading segments of MDs are the sources of stacking-fault generation as previously studied theoretically[37] and experimentally[38–40] in SiGe/Si heterostructures. According to the average measured size of the stacking-faults, the stacking-faults should extend from the interface, probably linked to a MD line, throughout to the island surface. In our island ensembles, the superdomes have shown to be full of defects. The presence of these defects is likely to alter the symmetry of the strain distribution, giving raise to undesired effects for possible electronic applications of these islands.

V. CONCLUSION

In summary, we have demonstrated that diffuse x-ray scattering around a bulk forbidden reflection is well suited to get complementary valuable information on defect size, distance between nearby dislocations, and atomic ordering in $Si_{1-x}Ge_x$ islands. The obtained x-ray results fit quite well with an independent determination by combining selective wet etching and extensive atomic force microscopy measurements. They provide important complementary information with respect to microscopy techniques such as AFM and TEM and information, which are not at all available by other techniques. Finally, we also show that plastic relaxation does not affect the appearance of atomic ordering, which in turn does not require a particular strain condition to be stabilized.

ACKNOWLEDGMENTS

All experiments were performed at beamline ID01 at the ESRF. We are very grateful to the ID01 staff for technical assistance and scientific considerations.

[1]G. Medeiros-Ribeiro, A. M. Bratkovski, T. I. Kamins, D. A. A. Ohlberg, and R. S. Williams, Science **279**, 353 (1998).
[2]T. I. Kamins, G. Medeiros-Ribeiro, D. A. A. Ohlberg, and R. S. Williams, J. Appl. Phys. **85**, 1159 (1999).
[3]R. S. Williams, G. Medeiros-Ribeiro, T. I. Kamins, and D. A. A. Ohlberg, Acc. Chem. Res. **32**, 425 (1999).
[4]F. M. Ross, R. M. Tromp, and M. Reuter, Science **286**, 1931 (1999).
[5]J. L. Gray, R. Hull, C. H. Lam, P. Sutter, J. Means, and J. A. Floro, Phys. Rev. B **72**, 155323 (2005).
[6]G. Biasiol and S. Heun, Phys. Rep. **500**, 117 (2011).
[7]M. S. Leite, G. Medeiros-Ribeiro, T. I. Kamins, and R. S. Williams, Phys. Rev. Lett. **98**, 165901 (2007).
[8]M. S. Leite, T. I. Kamins, R. S. Williams, and G. Medeiros-Ribeiro, J. Phys. Chem. C **116**, 901 (2012).
[9]A. Malachias, T. U. Schülli, G. Medeiros-Ribeiro, L. G. Cancado, M. Stoffel, O. G. Schmidt, T. H. Metzger, and R. Magalhaes-Paniago, Phys. Rev. B **72**, 165315 (2005).
[10]A. Malachias, M. Stoffel, M. Schmidbauer, T. U. Schulli, G. Medeiros-Ribeiro, O. G. Schmidt, R. Magalhaes-Paniago, and T. H. Metzger, Phys. Rev. B **82**, 035307 (2010).
[11]J. Z. Tischler, J. D. Budai, D. E. Jesson, G. Eres, P. Zscack, J. M. Baribeau, and D. C. Houghton, Phys. Rev. B **51**, 10947 (1995).
[12]G. Vantarakis, I. Remediakis, and P. C. Kelires, Phys. Rev. Lett. **108**, 176102 (2012).
[13]F. K. LeGoues, M. C. Reuter, J. Tersoff, M. Hammar, and R. M. Tromp, Phys. Rev. Lett. **73**, 300 (1994).
[14]M. Hammar, F. K. LeGoues, J. Tersoff, M. C. Reuter, and R. M. Tromp, Surf. Sci. **349**, 129 (1996).
[15]B. J. Spencer and J. Tersoff, Appl. Phys. Lett. **77**, 2533 (2000).
[16]B. J. Spencer and J. Tersoff, Phys. Rev. B **63**, 205424 (2001).
[17]T. Merdzhanova, S. Kiravittaya, A. Rastelli, M. Stoffel, U. Denker, and O. G. Schmidt, Phys. Rev. Lett. **96**, 226103 (2006).
[18]F. Boioli, V. A. Zinovyev, R. Gatti, A. Marzegalli, F. Montalenti, M. Stoffel, T. Merdzhanova, L. Wang, F. Pezzoli, A. Rastelli *et al.*, J. Appl. Phys. **110**, 044310 (2011).
[19]H. T. Johnson and L. B. Freund, J. Appl. Phys. **81**, 6081 (1997).
[20]D. J. Smith, D. Chandrasekhar, S. A. Chaperro, P. A. Crozier, J. Drucker, M. Floyd, M. R. McCartney, and Y. Zhang, J. Cryst. Growth **259**, 232 (2003).
[21]*X-Ray and Neutron Diffraction in Nonideal Crystals*, edited by M. A. Krivoglaz (Springer-Verlag, Berlin, 1996).
[22]P. Ehrhart, T. Trinkaus, and B. C. Larson, Phys. Rev. B **25**, 834 (1982).
[23]J. C. H. Spence, H. R. Kolar, G. Hembree, C. J. Humphreys, J. Barbard, R. Datta, C. Koch, F. M. Ross, and J. F. Justo, Philos. Mag. **86**, 4781 (2006).
[24]S. Takeno, M. Koike, H. Tanaka, T. Kinno, M. Tomita, and F. Uesugi, Surf. Interface Anal. **40**, 1655 (2008).
[25]P. H. Dederichs, Phys. Rev. B **4**, 1041 (1971).
[26]H. Trinkaus, Phys. Status Solidi B **51**, 307 (1972); **54**, 209 (1972).
[27]M. I. Richard, T. H. Metzger, V. Holý, and K. Nordlund, Phys. Rev. Lett. **99**, 225504 (2007).
[28]M. I. Richard, A. Malachias, J.-L. Rouvière, T.-S. Yoon, E. Holmström, Y.-H. Xie, V. Favre-Nicolin, V. Holý, K. Nordlund, G. Renaud *et al.*, Phys. Rev. B **84**, 75314 (2011).
[29]T. K. Carns, M. O. Tanner, and K. L. Wang, J. Electrochem. **142**, 1260 (1995).
[30]F. Wang, Y. Shi, J. Liu, Y. Lu, S. Gu, and Y. Zheng, J. Electrochem. Soc. **144**, L37 (1997).
[31]K. Koyama, M. Hiroi, T. Tatsumi, and H. Hirayama, Appl. Phys. Lett. **57**, 2202 (1990).
[32]E. Sutter, P. Sutter, and J. E. Bernard, Appl. Phys. Lett. **84**, 2262 (2004).
[33]B. C. Larson and W. Schmatz, Phys. Rev. B **10**, 2307 (1974).
[34]F. K. LeGoues, M. Copel, and R. M. Tromp, Phys. Rev. B **42**, 11690 (1990).
[35]A. Malachias, R. Magalhaes-Paniago, B. R. A. Neves, W. N. Rodrigues, M. V. B. Moreira, H.-D. Pfannes, A. G. de Oliveira, S. Kycia, and T. H. Metzger, Appl. Phys. Lett. **79**, 4342 (2001).
[36]M. I. Richard, A. Malachias, T.-U. Schülli, V. Favre-Nicolin, Z. Zhong, T.-H. Metzger, and G. Renaud, Appl. Phys. Lett. **106**, 012108 (2015).
[37]J. Zou and D. Cockayne, J. Appl. Phys. **74**, 925 (1993).
[38]Y. Kimura, N. Sugii, S. Kimura, K. Inui, and W. Hirasawa, Appl. Phys. Lett. **88**, 031912 (2006).
[39]P. Marée, J. Barbour, J. van der Veen, C. B.-L. K. L. Kavanang, and M. Viegers, J. Appl. Phys. **62**, 4413 (1987).
[40]S. Bedell, H. Chen, D. Sadana, K. Fogel, and A. Domenicucci, *A Survey of Defects in Strained Si Layers* (Mater. Res. Soc. Symp. Proc. 2004), Vol. 809, p. B1.5.1.